

Advanced 3D Monte Carlo algorithms for bio-photonic and medical applications

Lewis McMillan



University of
St Andrews

This thesis is submitted in partial fulfilment for the degree of
PhD
at the
University of St Andrews

March 2019

Contents

Abbreviations	iii
List of Figures	v
1 Computational modelling of tissue ablation	1
1.1 Introduction and background	1
1.2 Methods	2
1.2.1 Monte Carlo radiation transport (MCRT)	2
1.2.2 Heat transport	3
1.2.3 Tissue Damage	9
1.2.3.1 Introduction	9
1.2.3.2 Modelling coagulation damage	11
1.2.3.3 Modelling physical tissue damage	11
1.2.4 Validation	12
1.2.4.1 Heat transport validation	12
1.2.4.2 MCRT & heat transport validation	13
1.3 <i>In silico</i> results	14
1.3.1 Introduction	14
1.3.1.1 Optical & thermal properties	14
1.3.1.2 Computational speed up:	15
1.3.2 Results	16
1.3.2.1 Investigating ablation temperature, T_a	16
1.3.2.2 Investigating beam type	17
1.3.2.3 Investigating thermal damage	17
1.4 Conclusion	19
Appendix A Heat equation derivation	27

Abbreviations

T_a ablation temperature.

AMR adaptive mesh refinement.

FDM finite difference method.

MCRT Monte Carlo radiation Transfer.

OCT optical coherence tomography.

PDT photo-dynamic therapy.

List of Figures

- 1.1 Flowchart of the tissue ablation algorithm.
- 1.2 Red lines are photon paths within a voxel. Black lines photon paths out with the voxel. Red photon paths, weighted by μ_a , are summed up in order to calculate the absorbed energy within each voxel.
- 1.3 Discretisation of $f(x)$.
- 1.4 Finite difference method stencil for simple explicit scheme
- 1.5 Computational domain decomposition. Total computational domain (red outline) is evenly divided between cores in the CPU. This is done via layers of the domain in the z direction. Information is passed to/from cores via the 'halo swap' process (see Fig. 1.6).
- 1.6 Halo swapping. Process A updates the area in red and blue on the left. It updates the blue area which is sent to process B as B's 'halo'. Process B cannot update it's own halo, but rather updates the halo for process A.
- 1.7 Ablation of a dog aorta, as viewed under a microscope. Steam vacuoles are clearly visible either side of the ablation area. Carbonisation is also evident at the edges of the ablation fronts. Adapted from [15].
- 1.8 Comparison between analytical solution and numerical method at $t=0.1$ s.
- 1.9 Water absorption coefficient for wavelengths 0-12000nm [33]. Data shows that water is highly absorbing in the infra-red portion of the spectrum compared to the visible portion.
- 1.10 Simulation of 81 pixel beams. Figure shows a a slice through the optical properties at the end of the simulation. Yellow is unchanged tissue, and purple is completely ablated tissue. Figure shows that the ablation craters do not overlap one another.
- 1.11 Simulation of 70 W CO₂ ablative laser, with a circular beam profile. Crater depths as a function of pixel beam energy for various ablation temperature (T_a)'s.
- 1.12 Simulation of 70 W CO₂ ablative laser, with a Gaussian beam profile. Crater depths as a function of pixel beam energy for various T_a 's.
- 1.13 Tissue thermal damage around the ablation crater (white). Thermal tissue damage values of 3 refer to 3rd degree burns, 2 to 2nd, and 1 to 1st degree burns respectively. P is the power in Watts, T_a is the ablation temperature in Kelvin, and E_p is the energy per pixel beam in mJ .
- 1.14 Figure shows the maximum horizontal extent of thermal damage as a function of energy per pixel beam, for different T_a 's.
- 1.15 Figure shows the extent of burns inflicted by the laser as a function of depth. Lines are taken from the central point of the laser beam through the tissue. Coloured dashed lines are 30W laser and solid coloured lines are 70W laser. Both data sets plotted for ablation temperature of 420 °C, and pixel beam energy of 400 mJ

1.16 Figure shows the extent of burns inflicted by the laser as a function of depth. Lines are taken from the central point of the laser beam through the tissue. Coloured dashed lines are 30W laser and solid coloured lines are 70W laser. Both data sets plotted for ablation temperature of $420^{\circ}C$, and pixel beam energy of 400 mJ

Chapter 1

Computational modelling of tissue ablation

1.1 Introduction and background

Lasers are used in wide variety of medical procedures not limited to: coagulating scalpels, port wine stain removal, tattoo removal, hair removal, and skin rejuvenation [1–5]. One class of laser used in these procedures are ablative lasers. Ablative lasers are usually high powered lasers targeted at a specific chromophore in the skin, to partially or fully remove layers of skin. These types of lasers are commonly used for aesthetic procedures such as: skin rejuvenation [5], and removal of various diseases such as Rhinophyma [6] or lesions/nodules [7]. Ablative lasers have also been recently investigated as a means of better drug penetration into the skin for various therapies such as [photo-dynamic therapy \(PDT\)](#). The ablative laser ‘drill’ holes in the skin, which allows topical treatments to better diffuse into the skin [8].

One downside to using lasers to remove tissue, is that unlike a scalpel, where the surgeon has full control of the depth of the incision, ablative lasers are not as predictable. Lasers can also cause thermal damage to the surrounding areas, leading to potentially unwanted effects, though some applications of ablative lasers utilise the thermal damage, particularly aesthetic procedures [9].

Currently the only reliable method to measure the depth of the ablative holes, is via a biopsy, which is an invasive procedure. In this work an [optical coherence tomography \(OCT\)](#) system is used to measure the ablative crater non-invasively *in-vivo*. The OCT measurements are then compared to a computational model developed as part of this project. It is hoped this computational model could be used to predict the depth of the ablative crater when using a certain laser power for various different applications such as: laser assisted drug delivery, and various cosmetic applications.

This chapter examines using [Monte Carlo radiation Transfer \(MCRT\)](#) techniques coupled to a heat transfer simulation, in order to study the thermal damage to tissue due to fractional lasers. Fractionated ablative lasers are ablative lasers where the power is spread over several beams, such as to leave viable tissue around zones of damaged/necrotic tissue [10]. We present experimental work carried out on porcine tissue by our collaborators at the University of Dundee and the photobiology department at Ninewells hospital, along side our computational model of tissue ablation.

1.2 Methods

In order to replicate the experimental work *in silico*, the numerical model has three main portions. The first is the **MCRT** that models light transport through tissue so that we can calculate the laser energy deposited as a function of time and space. The second, a **finite difference method (FDM)** which is used to calculate the heat diffusion within the tissue due to the absorbed laser energy. Finally, a tissue damage model to track the tissue damage caused by the laser. All these individual portions are connected together to create our numerical model. This chapter explains in detail each portion of the numerical model used to simulate tissue ablation via a laser.

1.2.1 Monte Carlo radiation transport (MCRT)

MCRT is used here to calculate the energy deposited by the laser. This is then passed to the heat transport simulation, which calculates the heat diffusion in the medium. The algorithm for the three coupled simulations is presented in Fig. 1.1.

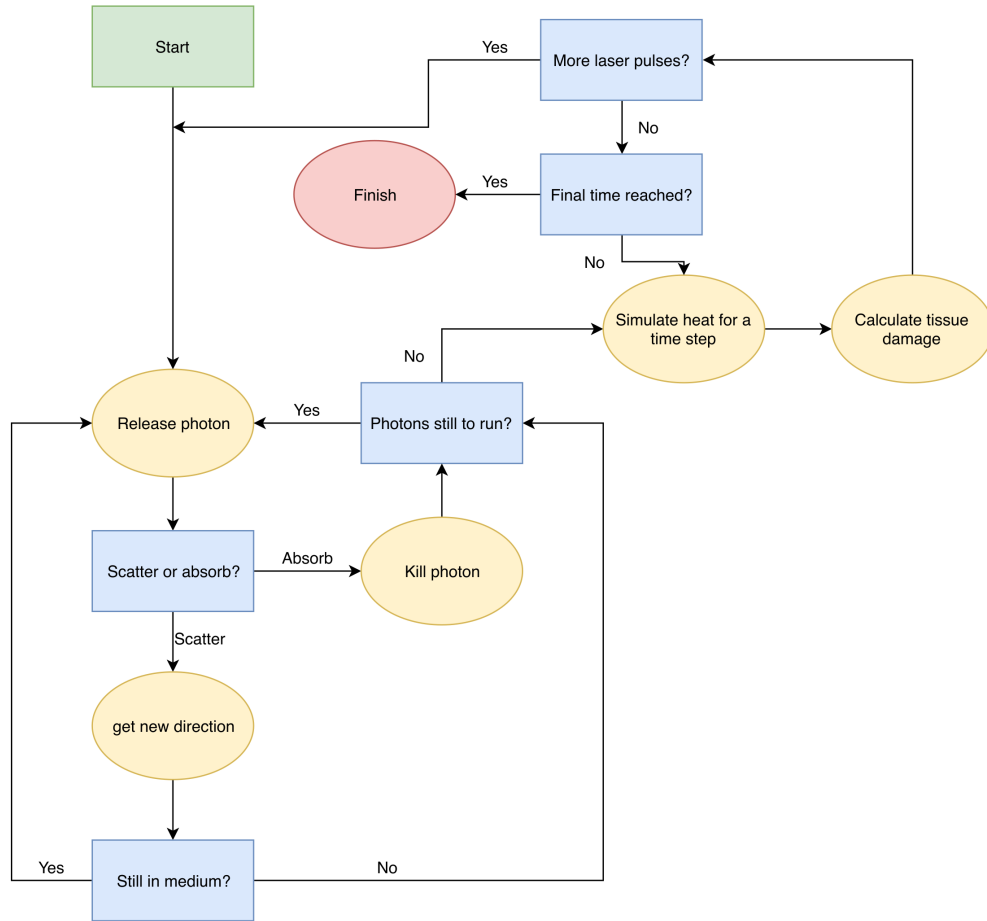


Figure 1.1: Flowchart of the tissue ablation algorithm.

The **MCRT** algorithm is largely the same as described in ??, with a couple of key adjustments.

The first adjustment to the algorithm is that the path length counter for fluence is adjusted to track absorbed energy instead. This is achieved by multiplying the pathlength in a voxel by the absorption coefficient of that voxel. Figure 1.2 show this process graphically, and Equation (1.36) shows the mathematical expression:

$$E_i^{abs} = \frac{P}{NV_i} \sum \mu_{a,i} s \quad (1.1)$$

Where:

P is power [W];

N is the number of photons;

V_i is the volume of the i^{th} voxel [m^{-3}];

$\mu_{a,i}$ is the absorption coefficient of the i^{th} voxel [cm^{-1}];

and s is the pathlength of a photon packet through the i^{th} voxel [cm].

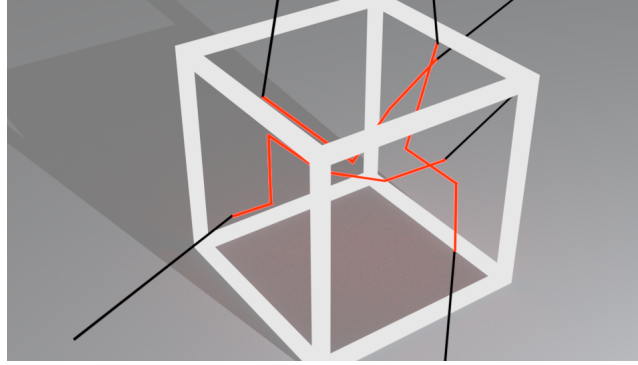


Figure 1.2: Red lines are photon paths within a voxel. Black lines photon paths out with the voxel. Red photon paths, weighted by μ_a , are summed up in order to calculate the absorbed energy within each voxel.

This grid of absorbed energy is then passed to the heat transport portion of the simulation, so that the heat diffusion in the porcine tissue can be calculated.

The next adjustment to the MCRT algorithm, is that the MCRT algorithm is run for every heat simulation time step. The simulation needs to be run for every time step, as the medium could change at every time step due to the optical, and thermal properties changing as a function of tissue damage.

Finally, to match the experiment undertaken the medium and laser for the *in-silico* experiments must match the ‘real life’ experiments. As the laser used in the experiments emits an infra-red wavelength, the optical properties are dominated by the water content of the tissue. Due to this we model just absorbing in the medium, with no scattering. Further discussion of this can be found in Section 1.3.1.1. The laser in some of the *in silico* experiments, has multiple beams. Thus the source photon routine is adjusted to accommodate this when needed.

1.2.2 Heat transport

The diffusion of heat can be modelled using the heat equation (Eq. (1.2)), which is derived from Fourier’s law and the principle of conservation of energy [11] (see Appendix A). The standard heat equation is a partial differential equation of the parabolic form. Solutions and analytical methods are readily available for lower dimensions (i.e. 1D heat diffusion), but for higher dimensions such

as three dimensions, numerical models must be used for all bar the simplest problems. The simplest form of the heat equation is shown below:

$$\rho c_p \frac{\partial T}{\partial t} = \nabla \cdot (\kappa \nabla T) + \dot{q} \quad (1.2)$$

Where:

- $T(x, y, z, t)$ is the temperature as a function of time and space $[K]$;
- κ is the thermal conductivity $[W \cdot m^{-1} \cdot K^{-1}]$;
- ρ is the density $[Kg \cdot m^{-3}]$;
- c_p the specific heat capacity $[J \cdot K^{-1}]$;
- $\dot{q}(x, y, z, t)$ is the source/sink term as a function of time and space $[W \cdot m^{-3}]$.

Equation (1.2) is for a homogeneous system where the thermal properties do not change as function of time, space and/or temperature. However in order to model a moving ablation front we must use the non-linear heat equation where the thermal properties can be a function of time, space and/or temperature (Eq. (1.3)).

$$\frac{\partial T}{\partial t} = \frac{1}{(\rho c_p)_\xi} (\nabla k_\xi T + k_\xi \nabla^2 T) + \dot{q} \quad \xi = (i, j, k) \quad (1.3)$$

We have also included in the Eq. (1.3) a source and sink term, \dot{q} to allow the modelling of heat loss/gain from external sources/sinks. The heat source in this simulation is due to the laser, and we assume the only loss of heat to the surrounding medium is via convection and conduction.

All faces of the cube, bar the laser facing face, are considered to be pinned at 5°C , as the porcine skin was kept cooled prior to experimental work and the simulation volume is smaller than the porcine tissue samples. The face of the medium on which the laser is incident, has a simple convective BC (based upon Newtons law of cooling):

$$\dot{q}_c = -hA(T - T_\infty) \quad (1.4)$$

Where:

- h is the heat transfer coefficient $[W \cdot m^{-2} \cdot K]$;
- A is the area of the grid element, that is radiating/convecting heat away $[m^{-2}]$;
- and T , and T_∞ are the temperature in a voxel and the surrounding medium temperature respectively $[K]$.

As Eq. (1.3) is generally hard to solve in arbitrary geometries with complex boundary conditions we employ a numerical method to solve Eq. (1.3). The numerical method we employ is a **FDM**. The **FDM** is derived from the Taylor series, see Eq. (1.5).

A function $f(x)$ is discretised onto a grid with N nodes a distance Δx apart (see Fig. 1.3). We can then truncate and rearrange Eq. (1.5) and assume that the remainder term R_1 is sufficiently small enough, to yield an approximation for the first derivative of a function $f(x)$ at a point $x_0 + \Delta x$, see Eq. (1.6). ?? is the so called forward difference, due to it using a point in the ‘forward’ direction. We can also calculate the ‘backward’ and central difference terms by using a node at $x_0 - \Delta x$ for the backward difference Eq. (1.7b). The central difference (Eq. (1.7c)) is an average of the forward and backwards differences. We can also give expressions for the 2^{nd} derivatives for backward, forward and central (forward and backward 2^{nd} order equations omitted for brevity) Eq. (1.7d).

$$f(x_0 + \Delta x) = f(x_0) + \frac{f'(x_0)}{1!} \Delta x + \frac{f''(x_0)}{2!} \Delta x^2 + \dots + \frac{f^{(n)}(x_0)}{n!} \Delta x^n + R_n(x) \quad (1.5)$$

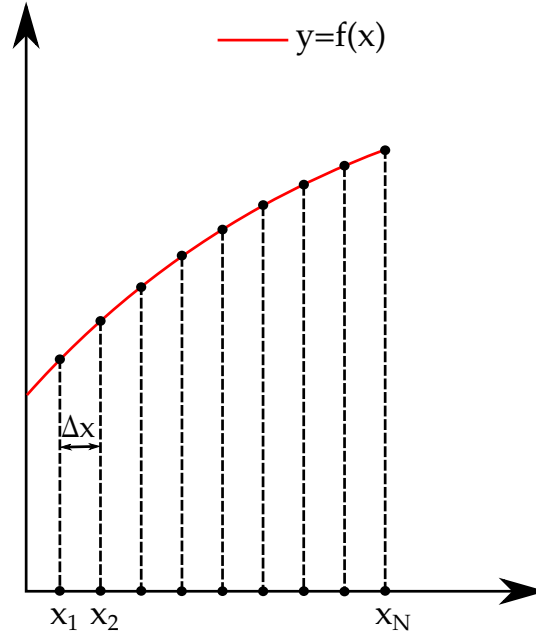


Figure 1.3: Discretisation of $f(x)$.

$$f'(x_0) \approx \frac{f(x_0 + \Delta x) - f(x_0)}{\Delta x} \quad (1.6)$$

$$\frac{df}{dx} = \frac{f_{i+1} - f_i}{\Delta x} \quad (\text{forward}) \quad (1.7a)$$

$$\frac{df}{dx} = \frac{f_i - f_{i-1}}{\Delta x} \quad (\text{backward}) \quad (1.7b)$$

$$\frac{df}{dx} = \frac{f_{i+1} - f_{i-1}}{2\Delta x} \quad (\text{central}) \quad (1.7c)$$

$$\frac{d^2f}{dx^2} = \frac{f_{i-1} - 2f_i + f_{i+1}}{\Delta x^2} \quad (\text{central}) \quad (1.7d)$$

Thus the linear heat equation Eq. (1.2), in 1D, taking a 1st order forward time derivative, and a 2nd order central spatial derivative gives:

$$\frac{T_i^{n+1} - T_i^n}{\Delta t} = \alpha \frac{T_{i-1}^n - T_i^n + T_{i+1}^n}{\Delta x^2} + \frac{\dot{q}}{\rho c_p} \quad (1.8a)$$

$$T_i^{n+1} = \alpha \Delta t \frac{T_{i-1}^n - 2T_i^n + T_{i+1}^n}{\Delta x^2} + \frac{\Delta t \dot{q}}{\rho c_p} \quad (1.8b)$$

Where $\alpha = \frac{\kappa}{\rho c}$.

*For brevity we define $f(x_0 + \Delta x)$ as f_{i+1} , $f(x_0 - \Delta x)$ as f_{i-1} , etc.

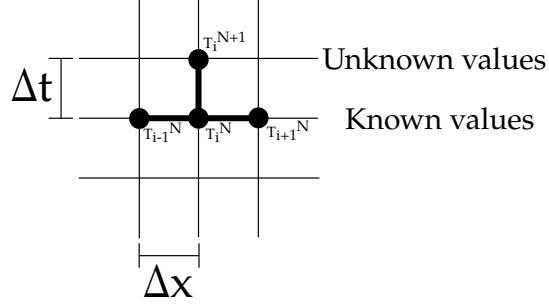


Figure 1.4: Finite difference method stencil for simple explicit scheme

Equation (1.8b) is called the ‘simple explicit form of finite-difference approximation’ [12]. Figure 1.4 shows the ‘stencil’ of this scheme, where there are three known points at time N , and just one unknown at time $N+1$. There are various other scheme that can be used to calculate the temperature at the the next time step. However we use a simple explicit scheme here, due to its ease of implementation despite there being a constraint on the stability in comparison to an implicit method. This method is also easily scaled up to 3D with little difficulty.

For the more complicated non-linear heat equation we have to account for the possibility that the medium is not continuously smooth between nodes, in terms of optical and thermal properties. The two easiest methods [12] of achieving this are: One, lag the value behind by one step, i.e $c_p^{n+1} = c_p^n$. Two, average κ , ρ , and c_p using a half difference scheme where the thermal property used in the calculation is the thermal property half way between two nodes, i.e the average of the two nodes:

$$\kappa^\pm = \frac{\kappa_i + \kappa_{i\pm 1}}{2} \quad (1.9)$$

$$\rho^\pm = \frac{\rho_i + \rho_{i\pm 1}}{2} \quad (1.10)$$

$$c_p^\pm = \frac{c_{p,i} + c_{p,i\pm 1}}{2} \quad (1.11)$$

Thus for the simple 1D case as in Eq. (1.8b), we average the thermal properties when computing the coefficients of the temperature nodes, and lag the thermal properties when adding the heat from the laser:

$$T^{N+1} = \Delta t (AT_{i-1}^N - 2BT_i^N + DT_{i+1}^N) + T_i^N + \frac{\Delta t \dot{q}_L}{\rho c_p} \quad (1.12)$$

Where (in the x direction):

$$\begin{aligned} A &= \frac{\kappa^-}{\rho^- c_p^- 2\Delta x^2} \\ B &= \frac{\kappa^+}{\rho^+ c_p^+ 2\Delta x^2} \\ D &= \frac{(A + B)}{2} \end{aligned} \quad (1.13)$$

Equation (1.12) can be generalised to higher dimensions easily. The 3D case gives:

$$U_{xx} = (AT_{i-1,j,k}^N - 2BT_{i,j,k}^N + DT_{i+1,j,k}^N) \quad (1.14)$$

$$U_{yy} = (AT_{i,j-1,k}^N - 2BT_{i,j,k}^N + DT_{i,j+1,k}^N) \quad (1.15)$$

$$U_{zz} = (AT_{i,j,k-1}^N - 2BT_{i,j,k}^N + DT_{i,j,k+1}^N) \quad (1.16)$$

$$T_{i,j,k}^{N+1} = \Delta t (U_{xx} + U_{yy} + U_{zz}) + T_{i,j,k}^N + \frac{\Delta t}{\rho c_p} \dot{q}_L \quad (1.17)$$

Where:

$T_{i,j,k}^{N+1}$ is the new temperature at node i, j, k [K];

$T_{i,j,k}^N$ is the temperature at node i, j, k at the current time step [K];

α is the thermal diffusivity [$m^2 \cdot s^{-1}$];

κ is the thermal conductivity [$W/m \cdot K$];

Δx etc. is the size of the grid element in the p^{th} direction [m];

and A, B, D are the coefficients in their respective dimension (Eq. (1.13)).

Incorporating B.Cs on the top air exposed face:

$$U_{zz} = \frac{\alpha}{\Delta z^2} \left(\frac{2\Delta z}{\kappa} (-h(T_{i,j,k}^N - T_{\infty}^N)) - 2T_{i,j,k}^N + 2T_{i,j,k+1}^N \right) \quad (1.18)$$

Equations (1.17) and (1.18) give the full numerical solution to the non-linear heat equation with a convection boundary term and laser heat source. This will allow us to calculate the heat diffusion in the porcine tissue due to laser heating.

As the laser used in the experimental work, operates in a pulsed mode, we account for this in our simulation. The laser pulse shape is a triangular pulse, with the peak power, P_{peak} , and pulse length, τ [13]. In the heat simulation we have an additional variable in the term $laserOn(t) \cdot \frac{\alpha \Delta t}{\kappa} \dot{q}_L$ in Eq. (1.17). This additional variable, $laserOn(t)$, is a boolean value and a function of time, which is defined as:

$$laserOn = \begin{cases} 1, & \text{Laser on} \\ 0, & \text{Laser off.} \end{cases}$$

In the instance where there is more than one pulse, the laser is turned on and off based upon the pulse frequency.

As we are using a simple explicit FDM, the time step is constrained in order to make the solution stable. For a cubic 3D FDM without prescribed flux BCs, yields the constraint: $\Delta t \leq \frac{1}{\delta \alpha}$ where $\delta = \frac{1}{\Delta x^2} + \frac{1}{\Delta y^2} + \frac{1}{\Delta z^2}$. However as there is also a convection boundary condition, the constraint on the timestep is more severe, due to the more mathematically complicated expressions [12].

However as we have a convection prescribed boundary condition, the constraint on the time is more severe. Along with this time constraint, the pulse length of the laser also has to be considered. If the time step of the heat simulation is too large it will not account for the heat deposited by the laser. Thus, the timestep has to be at least an order of magnitude smaller than the shortest laser pulse.

As the time step is small, and the grid resolution large, the resultant simulation is slow. Thus the code has been fully parallelised to improve performance. Both the MCRT and heat simulation are independently parallelised.

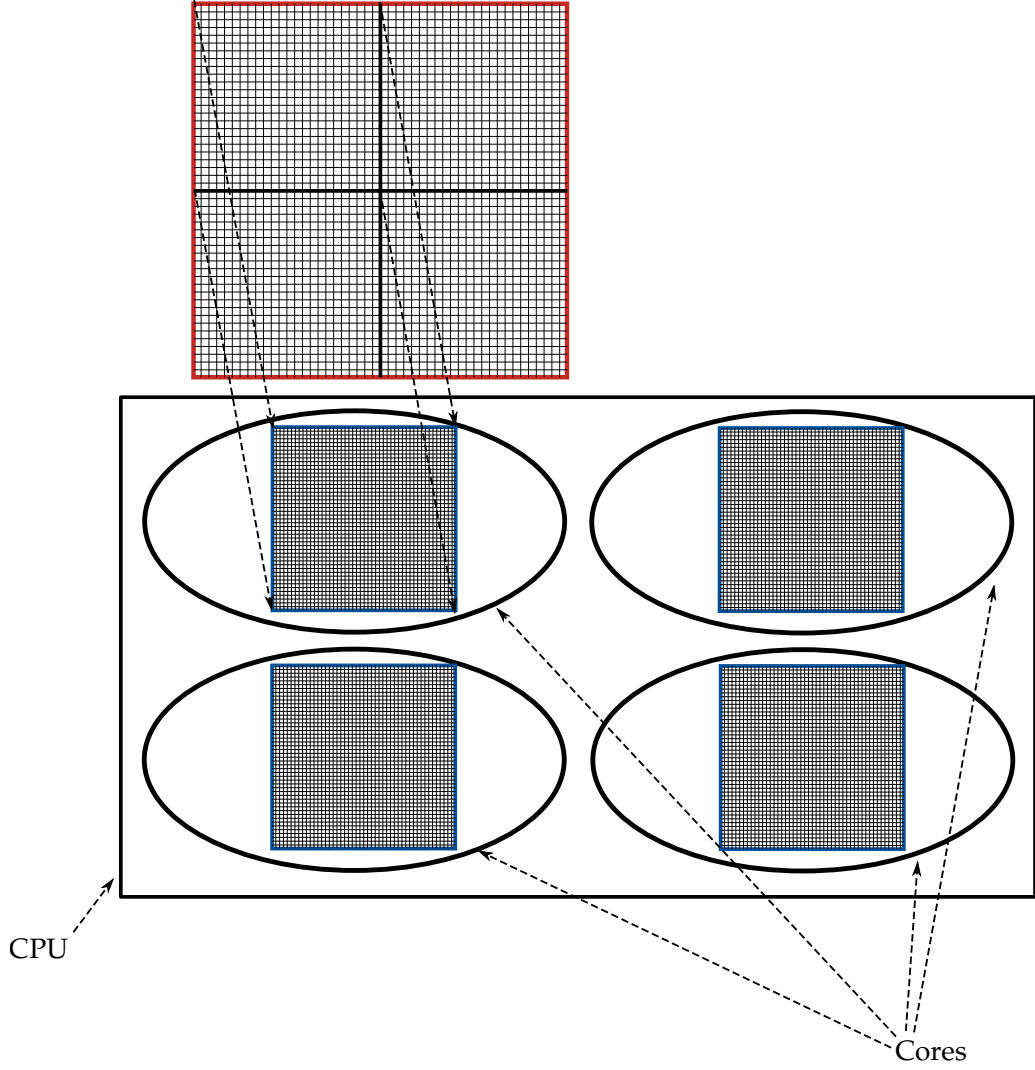


Figure 1.5: Computational domain decomposition. Total computational domain (red outline) is evenly divided between cores in the CPU. This is done via layers of the domain in the z direction. Information is passed to/from cores via the ‘halo swap’ process (see Fig. 1.6).

Parallelisation of the heat simulation is more involved than the ‘embarrassingly parallel’ class of problems that MCRT belongs to. This is due to the heat simulation being dependent on the temperature of adjacent nodes. Thus information will have to be passed from each individual core during computation, as opposed to doing the information passing at the end of the simulation *à la* MCRT parallelisation. The heat simulation is parallelised using a technique called ‘halo swapping’. This involves splitting up the computational domain (see Fig. 1.5), in this case the tissue medium, and doing the calculations on each domain on a separate core. The ‘halo swapping’ comes in when cores need to communicate with each other about updating their boundary temperature nodes (see Fig. 1.6).

* old data from before non-linear heat equation * On a workstation computer these simulations were carried out on (Intel Xeon E3-1245 v5, 8 core @ 3.5GHz) led to a speed up of ~ 6 , over the serial simulation. Using Amdahl’s law [14], the serial portion of the simulation is $\sim 5\%$, giving a theoretical speed up ~ 20 times the serial simulation.

After one time step of the heat simulation has been completed, the temperature grid is passed to the tissue damage portion of the simulation to calculate the tissue damage that may

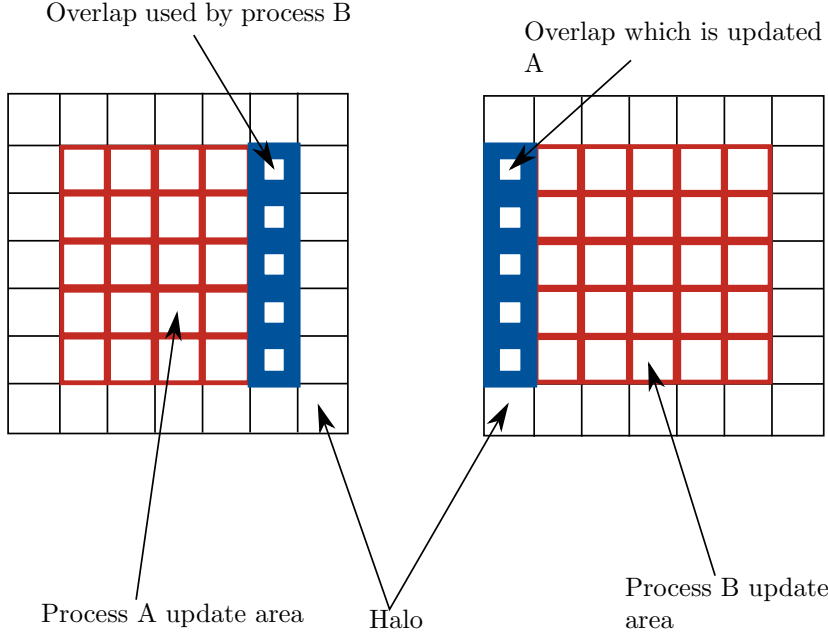


Figure 1.6: Halo swapping. Process A updates the area in red and blue on the left. It updates the blue area which is sent to process B as B’s ‘halo’. Process B cannot update it’s own halo, but rather updates the halo for process A.

have accrued during the heat simulation time step.

1.2.3 Tissue Damage

1.2.3.1 Introduction

The final portion of the simulation is the tissue damage model. To be able to model damage to the tissue we first need to be able to describe the tissue damage process due to heating from a laser.

When the laser is turned on, the temperature starts to rise within the tissue due to the absorption of photons by the tissue. The temperature rise causes damage to the tissue when above a threshold temperature, T_d , approximately 43°C [15]. From the temperature, T_d , we define four main areas of tissue damage:

$$T = \begin{cases} \text{coagulation,} & T_d \leq T \leq 100^\circ\text{C} \\ \text{water boils,} & T = 100^\circ\text{C} \\ \text{carbonisation,} & 100^\circ\text{C} \leq T \leq T_a \\ \text{ablation,} & T = T_a. \end{cases} \quad (1.19)$$

The area of tissue damage we term ‘coagulation’ is a multifaceted process. At 43°C - 50°C , bonds break within cell membranes, causing ruptures, and some cell death [15, 16]. This process is usually termed *hyperthermia*. Around 50°C , enzyme activity decreases, cells become immobile, and various cell repair mechanisms are disabled, leading to increased cell death. When temperatures exceed 60°C , proteins become denatured. Thermal denaturation is a structural and functional change in a protein due to the heating it undergoes. This means they change

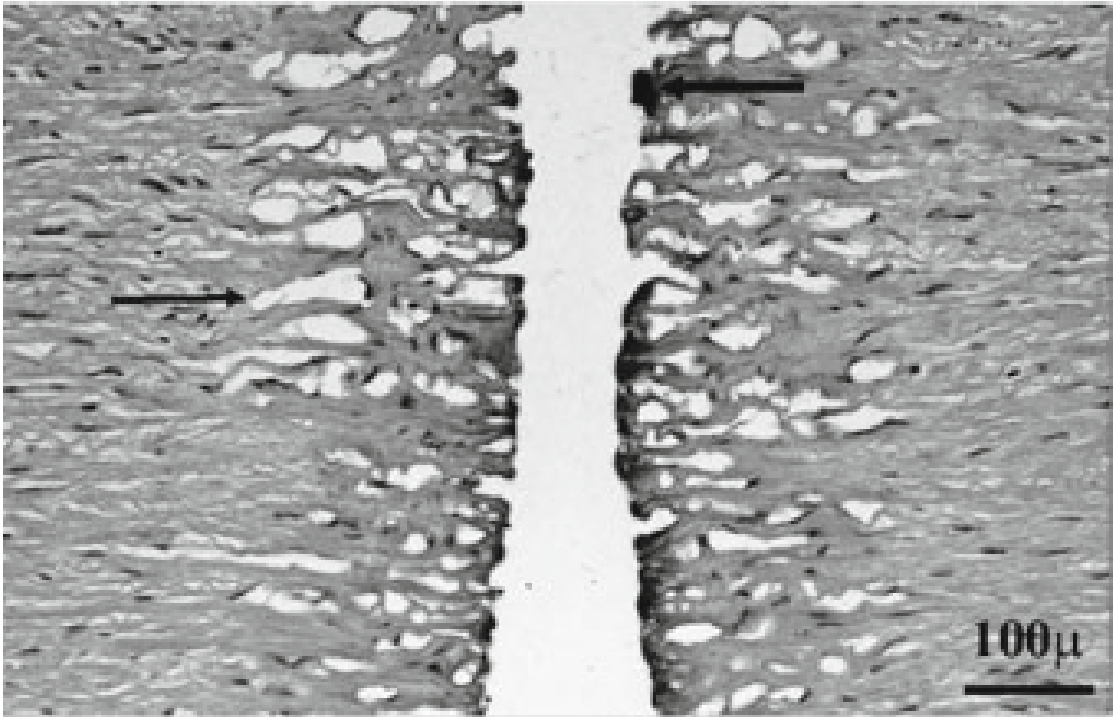


Figure 1.7: Ablation of a dog aorta, as viewed under a microscope. Steam vacuoles are clearly visible either side of the ablation area. Carbonisation is also evident at the edges of the ablation fronts. Adapted from [15].

from a highly organised structure with specific purposes, to disorganised structures with little to no function at all. [17]

The next stage in the tissue damage process is the vaporisation of water. As the temperature of the tissue starts to approach 100°C (at 1 atm), water starts to vaporise. If the vaporised water cannot escape the tissue it forms steam vacuoles, small pockets of steam. These vacuoles can easily be seen when viewing tissue samples after tissue has been treated with a high powered laser (see Fig. 1.7). In certain conditions these steam pockets can explode, with these ‘explosions’ being audible by the human ear [18].

The third stage of tissue damage is carbonisation or caramelisation of the tissue. This occurs when most of the water has boiled off, leaving the remaining tissue to heat up and reduce to its elemental carbon form. This carbonisation of tissue, when it occurs, is generally only a thin layer of $5\text{--}20\text{ }\mu\text{m}$ [15, 19].

The final stage of tissue damage is the removal of the remaining tissue, i.e tissue ablation. There is no agreement in the literature how tissue undergoes ablation with a number of methods proposed [20, 21]. The tissue ablation process is not a simple process, with various unknowns which depend on everything from tissue composition to laser power, wavelength, and pulse length. The literature however, does suggest that it takes place when the tissue temperature is between 177 and 500°C [22–24].

In order to model all these tissue damage processes we split our tissue damage model into two sections: ‘physical’ damage and coagulation damage. Where ‘physical’ damage changes the tissue optical and thermal properties, where the coagulation damage has no effect on the tissue’s bulk optical or thermal properties.

1.2.3.2 Modelling coagulation damage

With the description of the various process that tissue undergoes during ablation, we can now create a numerical model of these processes. First, in order to model the full extent of the damage done under 100°C, i.e in the coagulation regime, we use the Arrhenius damage model. The Arrhenius damage model was originally used as a kinetic model of reaction products in chemistry [25]. It has since been adapted by various authors for modelling tissue damage, and is the *de facto* standard [26, 27]. These authors and various others, adapted this model by fitting Eq. (1.20) to experimental data for burn damage. The two parameters fitted are A, the frequency factor, and ΔE , the activation energy.

$$\Omega(t) = \int_{t_i}^{t_f} A e^{(-\frac{\Delta E}{RT})} d\tau \quad (1.20)$$

Where:

- Ω is the damage value;
- A is ‘frequency factor’ [s^{-1}];
- ΔE is activation energy [$J \cdot mol^{-1}$];
- R is the universal gas constant [$J \cdot mol^{-1} \cdot K^{-1}$];
- T is the temperature [K];
- and t_i and t_f are the initial time and final time at t_{crit} .

It is reported that a value of Ω of 0.53, 1.0, and 10^4 relate to first, second, and third degree burns respectively [28]. We use the Arrhenius damage model in order to better understand the amount of damage caused by the laser in the non-ablated areas of tissue. We adopt of $A = 3.1 \times 10^{98}$, and $\Delta E = 6.27 \times 10^8$ for $T \leq 55$, and for $T > 55$ $A = 5 \times 10^{45}$, and $\Delta E = 2.96 \times 10^8$ [29].

1.2.3.3 Modelling physical tissue damage

As tissue mostly consists of water [30] when the temperature of the tissue approaches 100°C (at 1 atm), water in the tissue begins to boil off. This acts as a large heat sink for the absorbed laser energy, slowing down the rate of ablation. The energy required to boil the water is $Q_{vapor} = m_v \cdot L_v$, where m_v is the mass of a voxel, and L_v is the latent heat of vaporisation. The energy to boil off the water is provided via the laser and heat diffusing into the voxel:

$$Q_{vapor} = \underbrace{laserOn(t) \cdot \dot{q} \cdot \Delta t \cdot V_{i,j,k}}_{\text{laser heating}} + \underbrace{c \cdot M_{i,j,k} \cdot \Delta T}_{\text{heat diffusion}} \quad (1.21)$$

Where:

- Q_{vapor} is the current energy in Joules that has been used to boil off the water in the voxel [J];
- $laserOn$ is a boolean variable that determine if the laser is on or off $[-]$;
- \dot{q} is the energy absorbed by the voxel due to the laser [$W \cdot m^{-3}$];
- Δt is the timestep [s];
- $V_{i,j,k}$ is the volume of the voxel labelled i, j, k [m^3];
- c is the heat capacity of the voxel [$J \cdot K^{-1}$];
- $M_{i,j,k}$ is the mass of the the voxel labelled i, j, k [Kg];
- and ΔT is the change in temperature the voxel would undergo, if the water was not boiling off.

As water boils off, the water content of each voxel changes. This affects the absorption coefficient, density, thermal conductivity, and heat capacity. Each of these vary with water content per voxel [31];

$$W = W_{init} - \left(W_{init} \cdot \left(\frac{Q_{current}}{Q_{vaporisation}} \right) \right) \quad (1.22)$$

$$\rho = \frac{1000}{W + 0.649 \cdot P} \quad (1.23)$$

$$c_p = 4.2 \cdot 10^3 \cdot W + 1.09 \cdot 10^3 \cdot P \quad (1.24)$$

$$\kappa = \rho \cdot (6.28 \cdot 10^{-4} \cdot W + 1.17 \cdot 10^{-4} \cdot P) \quad (1.25)$$

$$\mu_a = W \cdot \mu_{water} + \mu_{protein} \quad (1.26)$$

$$(1.27)$$

Where:

W is the water content (i.e $W = 0.7$ equates to 70% water content);

W_{init} is the initial water content;

$Q_{current}$ is the total energy absorbed by the i^{th} voxel since the temperature reached 100°C [J];

P is the protein content (i.e $P = 1.0 - W$);

κ is the Thermal conductivity [$W \cdot m^{-1} \cdot K^{-1}$];

c_p is the heat capacity [$J \cdot Kg^{-1} \cdot K^{-1}$];

and μ_a is the total absorption coefficient, and μ_{water} and $\mu_{protein}$ are the absorption coefficients of water and protein respectively.

We define the T_a as occurring between 177 and 500°C [22–24]. At T_a the tissue is removed and the thermal, optical, and physical properties set to that of air.

The updated damaged tissue structure is then fed back to the MCRT model and the whole process repeats until the predefined time limit is reached. This whole process of photon propagation, heat diffusion and tissue damage is outlined in Fig. 1.1.

1.2.4 Validation

1.2.4.1 Heat transport validation

In order to thoroughly validate the numerical method we employ to solve the heat equation, we compare the numerical method against an easily solvable analytical case. We solve the heat equation on a cube, side L , in a surrounding medium of 0°C. The cube is initially at temperature 37°C and we calculate the temperature at time $t=0.1s$. Thus the boundary conditions are:

$$T(0, y, z, t) = T(x, 0, z, t) = T(x, y, 0, t) = 0^\circ C \quad (1.28)$$

$$T(L, y, z, t) = T(x, L, z, t) = T(x, y, L, t) = 0^\circ C \quad (1.29)$$

The thermal diffusivity (α), density (ρ), and heat capacity (c_p) are all set to 1. Assuming a separable solution in Cartesian coordinates yields:

$$\begin{aligned} T(x, y, z, t) = & (A_1 \cos(\alpha x) + A_1 \sin(\alpha x)) \cdot \\ & (B_1 \cos(\beta y) + B_1 \sin(\beta y)) \cdot \\ & (C_1 \cos(\gamma z) + C_1 \sin(\gamma z)) \cdot e^{-\alpha \mu^2 t} \end{aligned} \quad (1.30)$$

$$\mu^2 = \alpha^2 + \beta^2 + \gamma^2 \quad (1.31)$$

Applying the boundary conditions (Eqs. (1.28) and (1.29)) gives:

$$A_1 = B_1 = C_1 = 0 \text{ and } \alpha = \frac{\pi n}{L} \quad \beta = \frac{\pi m}{L} \quad \gamma = \frac{\pi p}{L} \quad (1.32)$$

$$\therefore T_{nmp}(x, y, z, t) = A_{nmp} \cdot \sin\left(\frac{\pi nx}{L}\right) \cdot \sin\left(\frac{\pi my}{L}\right) \cdot \sin\left(\frac{\pi pz}{L}\right) \quad (1.33)$$

This yields the following solution for the heat equation using the principle of superposition, and solving Eq. (1.34) with $f(x, y, z)$ as the initial temperature profile of the cube:

$$A_{nmp} = \frac{8}{L^3} \int_0^L \int_0^L \int_0^L f(x, y, z) \cdot \sin\left(\frac{\pi nx}{L}\right) \cdot \sin\left(\frac{\pi my}{L}\right) \cdot \sin\left(\frac{\pi pz}{L}\right) dx \cdot dy \cdot dz \quad (1.34)$$

$$T(x, y, z, t) = \sum_{n=1,3,\dots}^{\infty} \sum_{m=1,3,\dots}^{\infty} \sum_{p=1,3,\dots}^{\infty} \frac{2368}{\pi^3 nmp} \cdot \sin\left(\frac{\pi nx}{L}\right) \cdot \sin\left(\frac{\pi my}{L}\right) \cdot \sin\left(\frac{\pi pz}{L}\right) \cdot e^{(-\lambda^2 t)} \quad (1.35)$$

Where:

$\lambda^2 = \alpha\pi^2\left(\frac{n^2}{L^2} + \frac{m^2}{L^2} + \frac{p^2}{L^2}\right);$
 n, m, p are odd integers;
and L is the length of the cube.

At time, $t = 0.1s$, a slice through the middle of the cube, $L = 1 \text{ cm}$, yields Fig. 1.8, which shows that the numerical method matches the analytical solution closely.

1.2.4.2 MCRT & heat transport validation

As a first test of our code, both MCRT and heat simulation, we compare to a simple analytical model of ablation. The simple model of ablation is as: We define the ablation energy (E_a) as the minimum energy required to raise the temperature of the medium to 100 °C, and then boil off the water in a volume dV , mass M . Thus in one dimension we have Eq. (1.36), where the symbols have their usual meanings. If the energy for ablation is delivered in a time dt by a laser of power density (Wcm^{-2}), P , this gives Eq. (1.37). Equation (1.37) can be rearranged in order to give an ablation front velocity, Eq. (1.38).

$$E_a = c_p \rho dx \Delta T + L_v \rho dx \quad (1.36)$$

$$P \cdot dt = \rho dx (c_p \Delta T + L_v) \quad (1.37)$$

$$u = \frac{P}{\rho(c_p \Delta T + L_v)} \quad (1.38)$$

Assuming the ablation front moves with constant velocity during the ablation, and using $L_v = 2.53 \cdot 10^6 \text{ J} \cdot \text{Kg}^{-1}$, $c_p = 4181 \text{ J} \cdot \text{Kg}^{-1} \cdot \text{K}^{-1}$ and the medium is a cube side 2 mm , with a starting temperature is 37 °C with a water content of 70% giving a density of $700 \text{ Kg} \cdot \text{m}^{-3}$. For these parameters this gives an ablation velocity, $u \simeq 0.77 \text{ cm} \cdot \text{s}^{-1}$, and a time to ablate through 2 mm of tissue of $\simeq 0.26 \text{ s}$. As the code developed in this chapter simulates the diffusion of heat in a medium due to an incident laser, the expected time to ablate through the same medium should be slightly less as heat diffuses away from the voxel while it is heated being heated. When the full heat + MCRT code is used to simulate this experiment, it gives a time, $t \simeq 0.33 \text{ s}$.

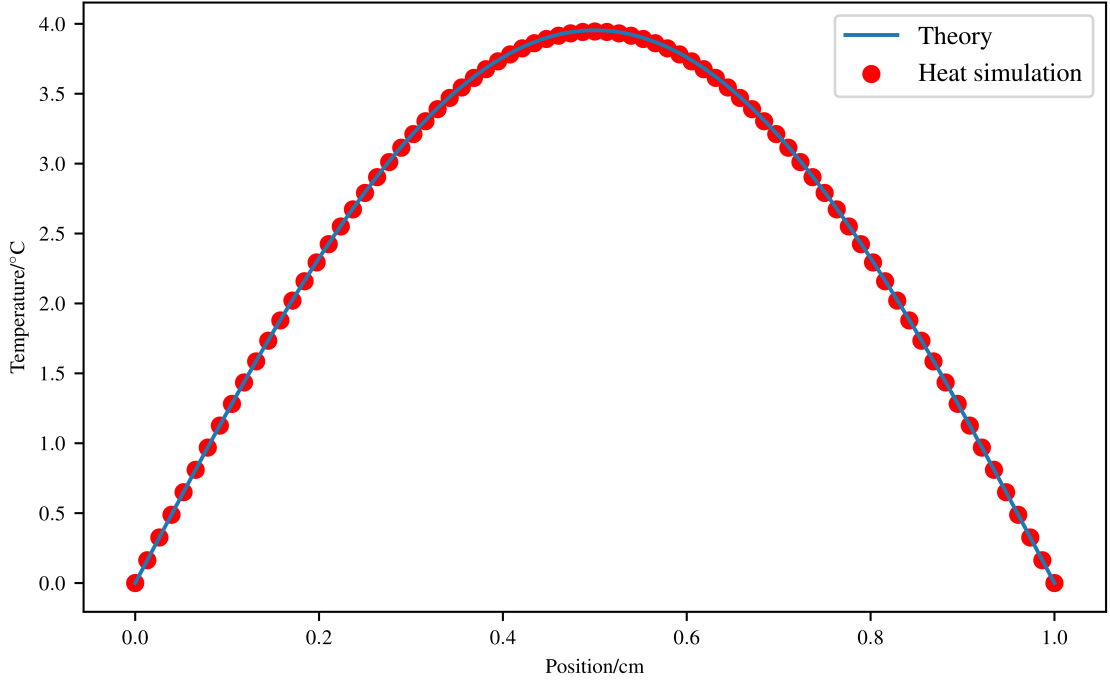


Figure 1.8: Comparison between analytical solution and numerical method at $t=0.1$ s.

1.3 *In silico* results

1.3.1 Introduction

In order to match the experimental results, we must first create as accurate model of the experimental setup *in silico*. However due to computational constraints, such as memory and time available, we must make some approximations to the experimental set-up. The porcine skin was a large thin slice of the top most layers of the skin. However as the area of interest is where the ablation occurs, we initially model the porcine skin as a cuboid, dimensions: $1.1 \times 1.1 \times 0.5$ cm. The initial temperature of the porcine skin is assumed to be around 5° , as the tissue was kept on ice or was kept cooled. As mentioned in the previous sections, there are several unknowns in the model: T_a , water content, temperature of air after ablation, and the exact thermal and optical properties of the porcine tissue. Therefore we run several models so that the full parameter space of these unknowns can be explored. Results from these *in silico* experiments are presented in this section along with a comparison of the model to the experimental work carried out in collaboration with the University of Dundee and the Photobiology department at Ninewells hospital.

1.3.1.1 Optical & thermal properties

The thermal and optical properties of porcine tissue are not known exactly for any given tissue sample. As such the thermal and optical properties used in this section are taken from various literature sources.

The laser used in the experimental work is an CO_2 laser operating at $10.6 \mu\text{m}$. This means that the optical properties of the tissue are dominated by water absorption (see Fig. 1.9). The laser used in the experiment is the Pixel CO_2 [32]. The Pixel CO_2 laser has a wavelength $10.6 \mu\text{m}$ which corresponds to an absorption of coefficient in water of $\sim 850 \text{ cm}^{-1}$. As the absorption coef-

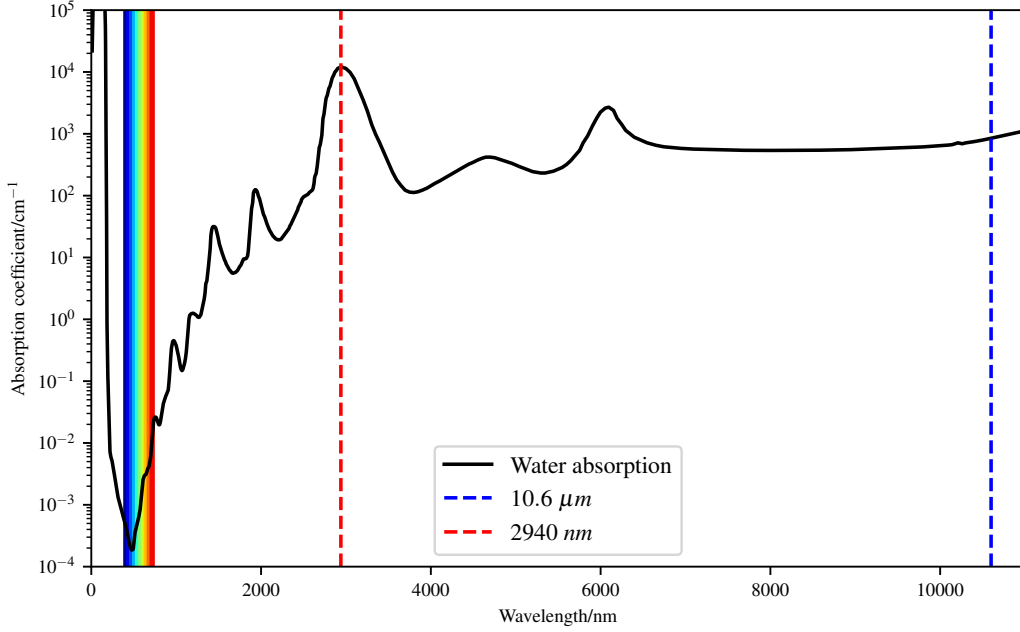


Figure 1.9: Water absorption coefficient for wavelengths 0-12000nm [33]. Data shows that water is highly absorbing in the infra-red portion of the spectrum compared to the visible portion.

	Thermal conductivity, κ	Density, ρ	Heat capacity, c
Tissue	$\rho \cdot (6.28 \cdot 10^{-4} \cdot W + 1.17 \cdot 10^{-4} \cdot P)$	$\frac{1000}{W+0.649 \cdot P}$	$4.2 \cdot 10^3 \cdot W + 1.09 \cdot 10^3 \cdot P$
Air	$ae^{-b(T-273.15)} + c$	$\frac{P_{atm}}{R_{spec}T}$	1006

Table 1.1: Optical and thermal properties for porcine tissue and air.

ficient is large, we assume that scattering is negligent at these wavelengths. Table 1.1 summarises the thermal properties for tissue and air used in the simulations.

The laser was used in ‘Pixel beam’ mode. This means that the laser beam is split into an array of smaller beams. The laser used an array 9×9 of 81 pixel beams, each with a spot size of $250 \mu m$. The Pixel CO₂ laser was upgraded during the period in which the experimental data was taken, we present both sets of data, pre-upgrade and post-upgrade. The upgrade consisted of an update to the laser power, from $\sim 30 W$ to $\sim 70 W$.

The laser delivered one single pulse of varying total energy delivered over the range $50 mJ$ to $400 mJ$, in so called “super pulsed mode”. The experiment consisted of ablating the porcine tissue, as a function of energy per ‘pixel’ beam. This was achieved by adjusting the pulse length of the laser, τ , so that the energy per pulse was varied over a range $50 mJ$ to $400 mJ$. The energy range for the laser was kept the same pre and post-upgrade, with the pulse length differing.

1.3.1.2 Computational speed up:

As discussed in the Section 1.1, the volume of interest is the area around the ablation craters. The volume is $1.1 \times 1.1 \times 0.5 cm$. However, in order for the simulation to have good resolution

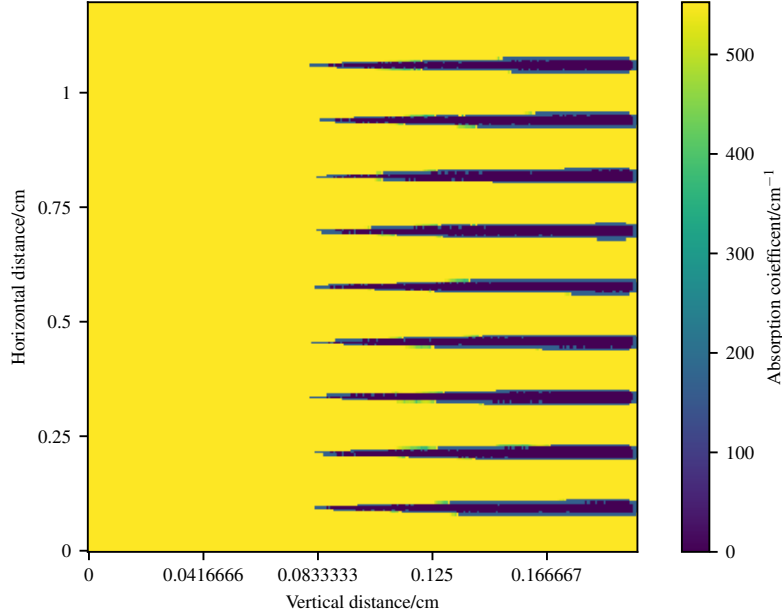


Figure 1.10: Simulation of 81 pixel beams. Figure shows a slice through the optical properties at the end of the simulation. Yellow is unchanged tissue, and purple is completely ablated tissue. Figure shows that the ablation craters do not overlap one another.

of the ablation craters, this volume would require a large number of voxels for the tissue model. This is unfeasible due to: the memory required to store the various counters, grids, and variables, and the time that would be required in order to carry out the computation. Thus the volume of interest is reduced to focus on just one of the ablation craters that is created by the laser. As a sanity check to ensure that we are not omitting any phenomena by focusing on just one ablation crater, an initial simulation that simulates the full volume of interest was carried out to investigate the possibility of overlapping craters or other related phenomena. The simulation, as shown in Fig. 1.10, gives us validation that the shrinking of the volume of interest is a valid approximation to make.

1.3.2 Results

1.3.2.1 Investigating ablation temperature, T_a

Various literature sources report the ablation temperature ranging from 177° to 500° [22–24]. Thus, we run several models over this range in order to establish a ‘good’ T_a which fits with the experimental results. Figures 1.11 and 1.12 show how T_a , and beam profile affect the crater depth as a function of pixel beam energy for the CO₂ laser. Simulation data suggests that, that a ‘good’ T_a is around $T_a = 450$ °C.

Increasing the ablation temperature, has the obvious affect of requiring more energy to be deposited by the laser before ablation takes place. This also allows more heat to diffuse away from the ablation crater increasing the thermal damage done to the surrounding tissue. Decreasing the ablation temperature has the converse affect, and allows the ablation crater to become deeper.

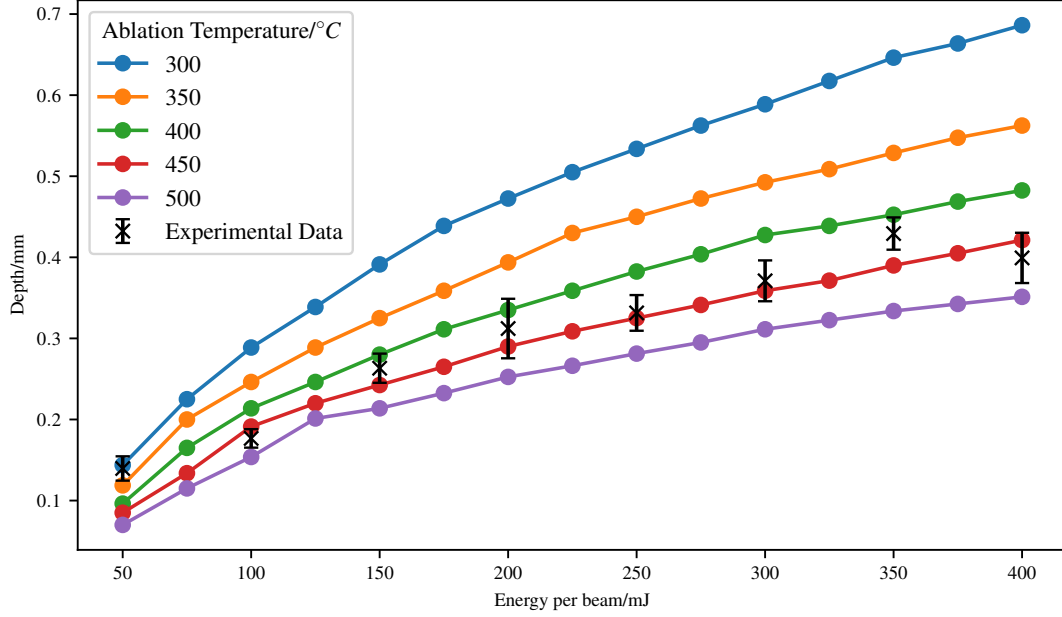


Figure 1.11: Simulation of 70 W CO_2 ablative laser, with a circular beam profile. Crater depths as a function of pixel beam energy for various T_a 's.

Over the full range of T_a , as the energy per pixel beam increases, there is a trend that at higher energies the crater depth tapers off. This is potentially due to a number of reasons. As the ablation craters grows the volume of tissue that is ablated is replaced with air, allowing more heat loss from the tissue to the environment. As well as heat loss to the environment, more heat is diffused away into the surrounding tissue as the crater grows, due to the availability of more tissue for the heat to diffuse into.

1.3.2.2 Investigating beam type

As the manufacturer does not provide information on the beam profile of the pixel beams, we have to assume the shape of the beam profiles. We tried two different shapes: Gaussian, and circular. Figures 1.11 and 1.12 show the result of these *in-silico* experiments. The Gaussian beam ablates deeper holes than the circular beam type, which is to be expected due to the distribution of power in the Gaussian beam. The beam that best fits the data, is the circular beam. For the Gaussian beam to fit the data 'well' ablation would have to take place at temperatures above 500°C which does not fit with the literature. Without knowing the exact profile of the beam, we assume for the rest of the *in-silico* experiments that the beam profile is circular.

1.3.2.3 Investigating thermal damage

As stated in Section 1.2.3.2, we use the Arrhenius damage integral in order to estimate the thermal damage due to the laser. In order to calculate the tissue damage around the ablation craters, we first transform Eq. (1.20) in to a summation:

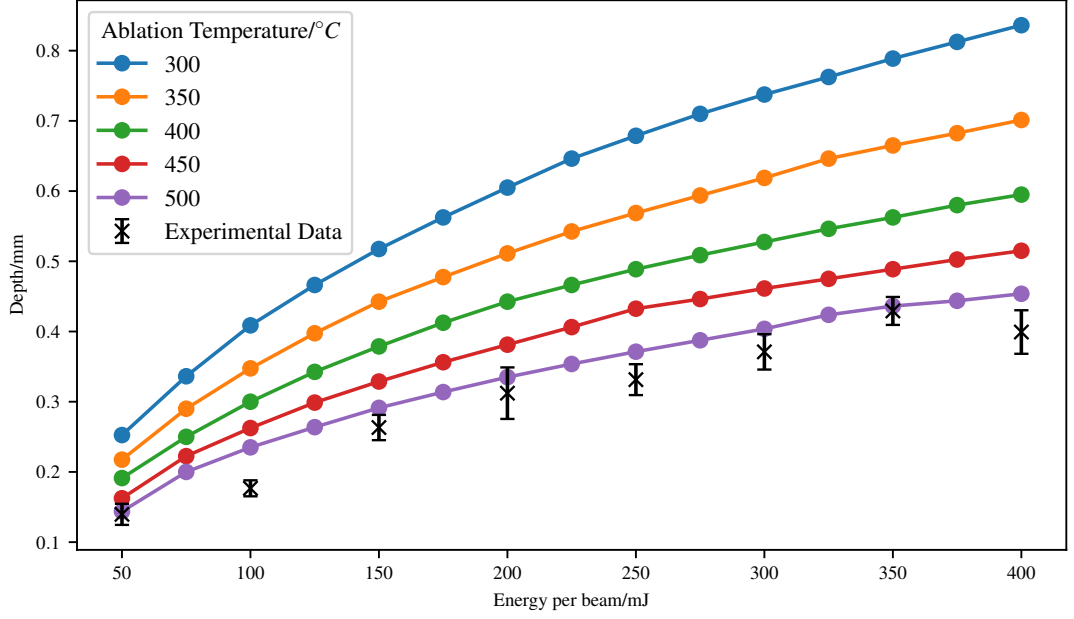


Figure 1.12: Simulation of 70 W CO₂ ablative laser, with a Gaussian beam profile. Crater depths as a function of pixel beam energy for various T_a 's.

$$\Omega(t) = \int_{t_p}^{t_f} A e^{(-\frac{\Delta E}{RT})} d\tau \quad (1.39)$$

$$\Omega(t) = \sum_{m=m_p}^{m_f} A e^{(-\frac{\Delta E}{RT_{\xi}^m})} \Delta t \quad (1.40)$$

Where:

ΔE , R , T , and A have the same meanings as before;

ξ is the i^{th}, j^{th}, k^{th} node;

and m_p is the p^{th} timestep when the ξ^{th} node is above the threshold temperature.

Using Eq. (1.40) we can thus estimate the damage to the tissue on a voxel by voxel basis. Figure 1.13 show how far the thermal damage extends around the ablation crater. For ease of visualisation we map 1-3 to their respective burns via the following scheme, with η as burn severity:

$$\eta = \begin{cases} 3, & \Omega \geq 10000 \\ 2, & 1 \leq \Omega < 10000 \\ 1, & 0.53 \leq \Omega < 1 \\ 0, & 0.0 \leq \Omega < 0.53. \end{cases} \quad (1.41)$$

As shown in Fig. 1.13, the thermal damage zone extends for a small distance around the ablation crater, due to the diffusion of heat into these areas.

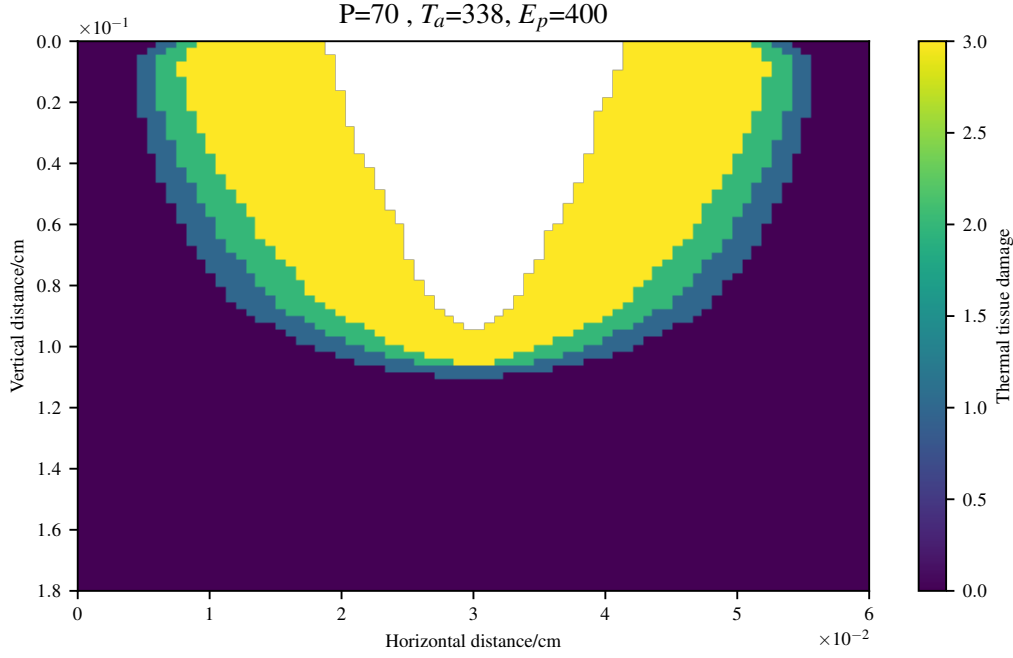


Figure 1.13: Tissue thermal damage around the ablation crater (white). Thermal tissue damage values of 3 refer to 3rd degree burns, 2 to 2nd, and 1 to 1st degree burns respectively. P is the power in Watts, T_a is the ablation temperature in Kelvin, and E_p is the energy per pixel beam in mJ.

We can also investigate the time it takes for different areas of the tissue to become thermally damaged. This can be easily achieved by saving the time each voxel passes one of the damage boundaries in Eq. (1.41). ?? show the minimum time taken for 1st, 2nd, and 3rd degree burns to occur for both 30 W and 70 W powered lasers as a function of depth. The 70 W laser shows that there is little to no time (upon the order of 0.5 ms) between 1st and 2nd degree burns, and a maximum of ~ 0.02 s between 2nd and 3rd degree burns. The 30 W has a larger time differential between burn classifications, with a maximum of 0.02 s between 1st and 2nd degree burns and a maximum of 0.2 s between 2nd and 3rd degree burns. The spatial distance between burn boundaries are also drastically different between the two different powers of laser. At 70W there is virtually no difference in the boundaries for the 1st and 2nd degree burns, with a slight difference of $\sim 5 \mu\text{m}$ between the 2nd and 3rd degree burns. 30 W the distance between 2nd and 3rd is $\sim 11 \mu\text{m}$, and for 1st and 2nd $\sim 1 \mu\text{m}$.

1.4 Conclusion

Using MCRT and finite difference method, we have created a fully 3D model of photon and heat transport within tissue. This model can be used to simulate the heat deposited by laser, the ablation craters formed via high powered laser and the resultant thermal damage surrounding the ablation crater.

Our model has been fully validated against both analytical solutions and experimental results.

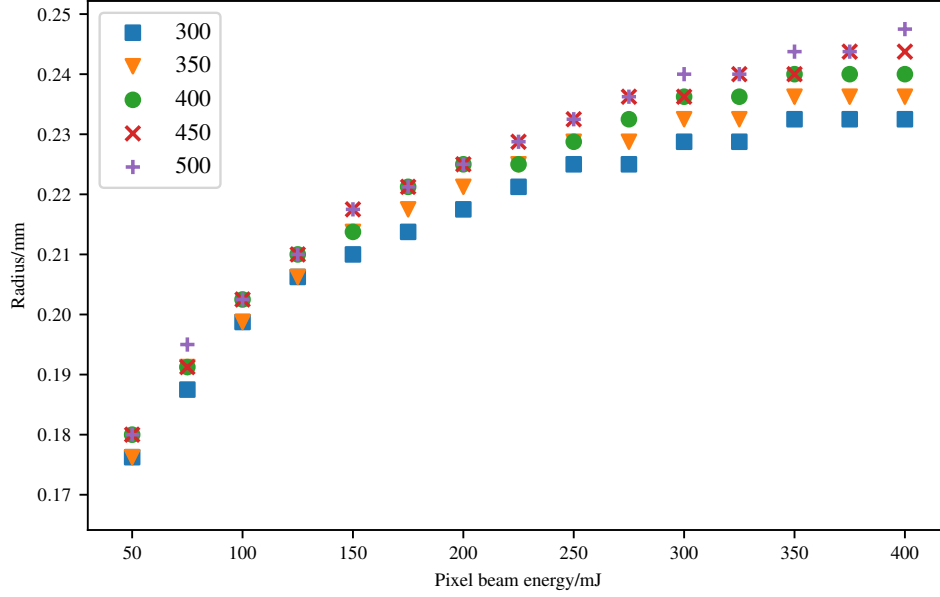


Figure 1.14: Figure shows the maximum horizontal extent of thermal damage as a function of energy per pixel beam, for different T_a ’s.

We found that to match with experimental results that a tissue ablation temperature T_a of around 420 K has to be adopted.

The simulations allow us to predict for a given laser power and pulse length, how much thermal damage is caused in the tissue, and how deep an ablation crater that will form. The computational model could be used in future to help develop treatment regimes for both aesthetic procedures. For example, currently there is a lot of ‘down time’ after skin rejuvenation, in which the patient displays inflammation, erythema, edema, pain, and crusting [34–36]. Simulations of thermal damage due to fractional ablation could help design treatment regimes that minimise these effects, whilst still delivering skin rejuvenation. The model can also be applied to help optimise laser assisted drug delivery. Laser assisted drug delivery consists of using a laser to ‘drill’ holes into the skin in order to help topical medicines diffuse into the skin better, than just applying the medicines to skin with no holes. Our model can help predict the laser parameters needed to reach a certain hole depth, thus minimising thermal damage and pain to patients.

There are many avenues available with regards to future work on this model. The model presented here in this chapter was on a initially homogeneous skin model. In reality skin is comprised of several distinctive layers, with each layer containing varying amounts of different chromophores. Our model can easily incorporate an n -layer skin model complete with various fractions of chromophores. The current model as present is a voxel based model, where all the voxels are the same size. This allows the model presented in this chapter to be easily set-up, with regards to parallelisation, optical/thermal properties and ease of programming. However voxel models, where all the voxels are the same size, are not computationally efficient. Particularly in order to achieve good resolution, many voxels are needed, which requires large amounts of RAM, due to a $\sim n^3$ scaling of voxels to memory in 3D. A more efficient way, would be to allow

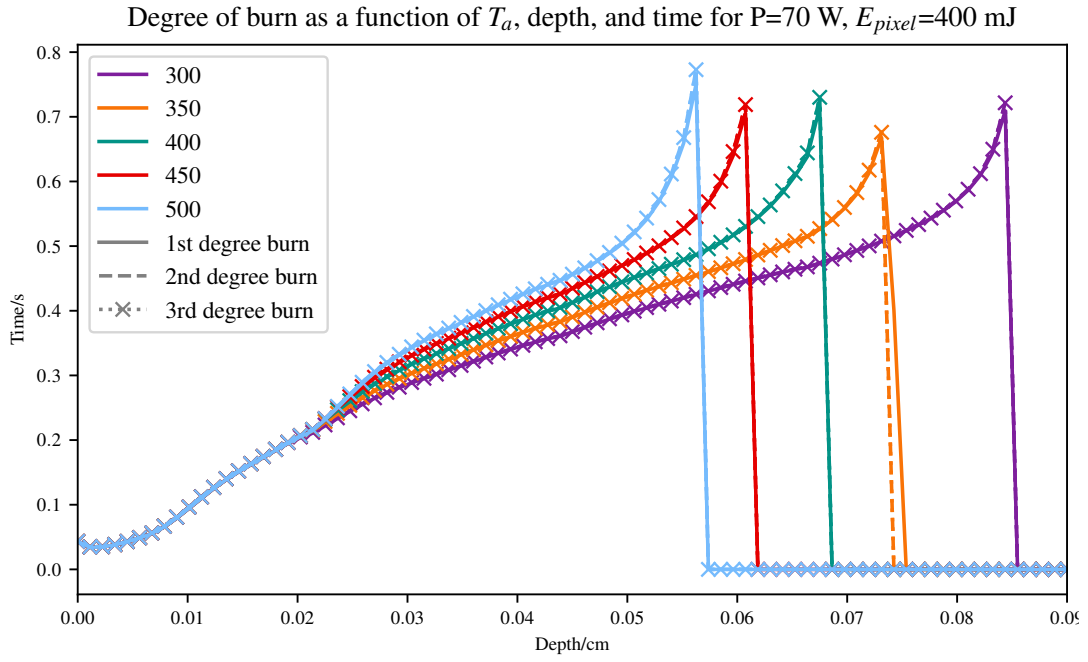


Figure 1.15: Figure shows the extent of burns inflicted by the laser as a function of depth. Lines are taken from the central point of the laser beam through the tissue. Coloured dashed lines are 30W laser and solid coloured lines are 70W laser. Both data sets plotted for ablation temperature of $420\text{ }^{\circ}\text{C}$, and pixel beam energy of 400 mJ

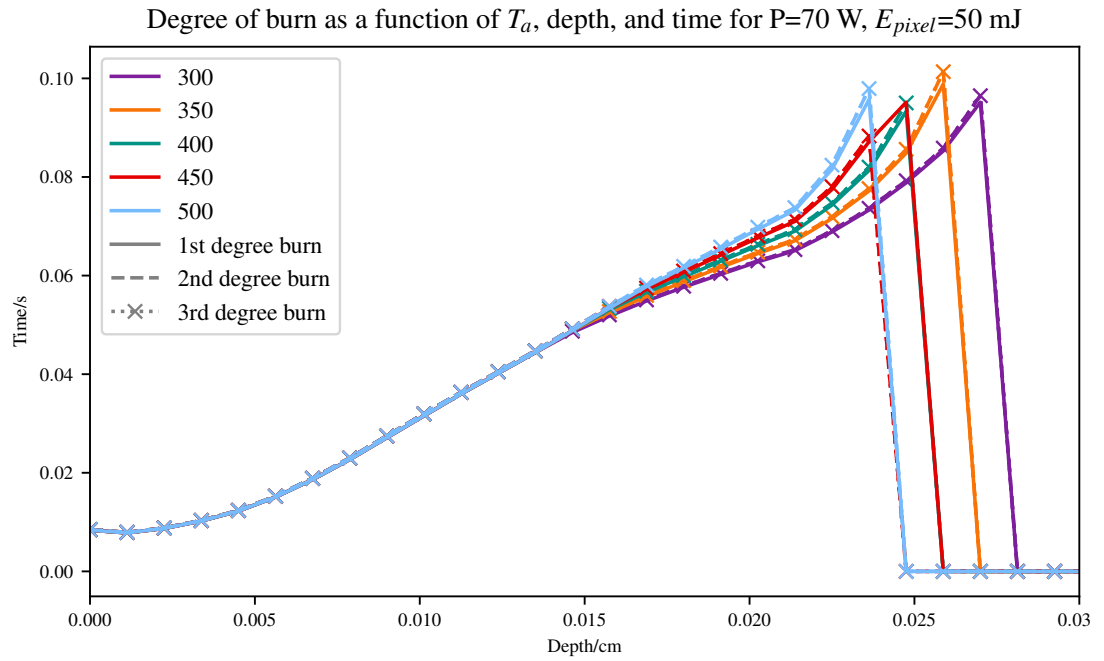


Figure 1.16: Figure shows the extent of burns inflicted by the laser as a function of depth. Lines are taken from the central point of the laser beam through the tissue. Coloured dashed lines are 30W laser and solid coloured lines are 70W laser. Both data sets plotted for ablation temperature of 420°C , and pixel beam energy of 400 mJ

different sizes of voxels, depending on parts of the model which need high resolution, and parts that do not need high resolution. Such a voxel model is called an [adaptive mesh refinement \(AMR\)](#). There are downsides to [AMR](#): complex implementation for parallelisation and set-up of optical/thermal, slower optical depth integration routines due to neighbour lookups.

Appendices

Appendix A

Heat equation derivation

To derive the heat equation we consider the conversation of energy in a volume R , with a flux out, $\phi(x, y, z, t)$, and unit outer normal $\hat{\mathbf{n}}$. We need just the normal component of ϕ : $\phi \cdot \hat{\mathbf{n}}$.

The rate of change of heat inside the volume R is equal to the heat generated inside the volume R plus the heat flowing in/out of the boundary surface:

$$\begin{array}{l} \text{Rate of change} \\ \text{of heat energy} \end{array} = \begin{array}{l} \text{Rate of heat} \\ \text{generation in} \\ R \end{array} + \begin{array}{l} \text{Rate of heat} \\ \text{flowing through} \\ \text{boundary surface} \end{array} \text{ energy} \quad (\text{A.1})$$

The total heat energy is:

$$e(x, y, z, t) = c(x, y, z) \cdot \rho(x, y, z) \cdot T(x, y, z, t) \quad (\text{A.2})$$

and therefore the rate of change of heat energy is

$$\frac{d}{dt} \iiint_R e \, dV = \frac{d}{dt} \iiint_R c\rho T \, dV \quad (\text{A.3})$$

We denote the heat generated inside the volume R as $Q(x, y, z, t)$:

$$\iiint_R Q \, dV \quad (\text{A.4})$$

and the rate of heat energy flowing through the boundary surface is:

$$- \iint_{\partial R} \phi \cdot \hat{\mathbf{n}} \, dS^\ddagger \quad (\text{A.5})$$

Substituting Eqs. (A.3) to (A.5) into Eq. (A.1), yields:

$$\frac{\partial}{\partial t} \iiint_R c\rho T \, dV = - \iint_{\partial R} \phi \cdot \hat{\mathbf{n}} \, dV + \iiint_R Q \, dV \quad (\text{A.6})$$

Using the divergence theorem, and simplifying gives:

[‡]This is negative as outward flow ϕ is positive, but the flow would result in a reduction of energy.

$$\frac{\partial}{\partial t} \iiint_R c\rho T \, dV = - \iiint_R \nabla \cdot \phi \, dV + \iiint_R Q \, dV \quad (\text{A.7})$$

$$\iiint_R \left[c\rho \frac{\partial}{\partial t} T + \nabla \cdot \phi - Q \right] dV = 0 \quad (\text{A.8})$$

Which holds for an arbitrary R , thus:

$$c\rho \frac{\partial}{\partial t} T = -\nabla \cdot \phi + Q \quad (\text{A.9})$$

Using Fourier's law of heat conduction, which states that the local heat flux density, ϕ , is proportional to the negative local temperature gradient. The proportionality constant being equal to the thermal conductivity, κ :

$$\phi(x, y, z, t) = \kappa(x, y, z) \nabla T(x, y, z, t) \quad (\text{A.10})$$

Substituting Eq. (A.10) into Eq. (A.9) yields the heat equation:

$$c\rho \frac{\partial}{\partial t} T = \nabla \cdot (\kappa \nabla T) + Q \quad (\text{A.11})$$

Which can be simplified into the homogeneous medium heat equation with the following assumptions: $Q=0$ and κ , ρ , and c are constant, and $\alpha = \frac{\kappa}{c\rho}$

$$\frac{\partial T}{\partial t} = \alpha \nabla^2 T \quad (\text{A.12})$$

Bibliography

- [1] S. Amini-Nik, D. Kraemer, M.L. Cowan, K. Gunaratne, P. Nadesan, B.A. Alman, and R.J. Dwayne Miller. Ultrafast mid-ir laser scalpel: protein signals of the fundamental limits to minimally invasive surgery. *PLoS One*, 5(9):e13053, 2010.
- [2] O.T. Tan, K. Sherwood, and B.A. Gilchrest. Treatment of children with port-wine stains using the flashlamp-pulsed tunable dye laser. *New England Journal of Medicine*, 320(7):416–421, 1989.
- [3] M. Kuperman-Beade, V.J. Levine, and R. Ashinoff. Laser removal of tattoos. *American Journal of Clinical Dermatology*, 2(1):21–25, 2001.
- [4] S.H. Liew. Laser hair removal. *American Journal of Clinical Dermatology*, 3(2):107–115, 2002.
- [5] C.A. Hardaway and E.V. Ross. Nonablative laser skin remodeling. *Dermatologic Clinics*, 20(1):97–111, 2002.
- [6] S.M. Shapshay, M.S. Strong, G.W. Anastasi, and C.W. Vaughan. Removal of rhinophyma with the carbon dioxide laser: a preliminary report. *Archives of Otolaryngology*, 106(5):257–259, 1980.
- [7] R. Valcavi, F. Riganti, A. Bertani, D. Formisano, and C.M. Pacella. Percutaneous laser ablation of cold benign thyroid nodules: a 3-year follow-up study in 122 patients. *Thyroid*, 20(11):1253–1261, 2010.
- [8] M. Hædersdal, F.H. Sakamoto, W.A. Farinelli, A.G. Doukas, J. Tam, and R.R. Anderson. Fractional CO₂ laser-assisted drug delivery. *Lasers in Surgery and Medicine: The Official Journal of the American Society for Laser Medicine and Surgery*, 42(2):113–122, 2010.
- [9] M.R. Alexiades-Armenakas, J.S. Dover, and K.A. Arndt. The spectrum of laser skin resurfacing: nonablative, fractional, and ablative laser resurfacing. *Journal of the American Academy of Dermatology*, 58(5):719–737, 2008.
- [10] D. Manstein, G.S. Herron, R.K. Sink, H. Tanner, and R.R. Anderson. Fractional photothermolysis: a new concept for cutaneous remodeling using microscopic patterns of thermal injury. *Lasers in Surgery and Medicine: The Official Journal of the American Society for Laser Medicine and Surgery*, 34(5):426–438, 2004.
- [11] D.V. Widder. *The Heat Equation*, volume 67. Academic Press, 1976.
- [12] N. Ozisik. *Finite Difference Methods in Heat Transfer*. CRC press, 1994.

- [13] Alma Lasers GmbH. *PixelCO2 Operator's Manual*. Alma Lasers GmbH.
- [14] G.M. Amdahl. Validity of the single processor approach to achieving large scale computing capabilities. In *Proceedings of the April 18-20, 1967, Spring Joint Computer Conference*, pages 483–485. ACM, 1967.
- [15] A.J. Welch, M.J.C. Van Gemert, et al. *Optical-thermal Response of Laser-irradiated Tissue*, volume 2. Springer, 2011.
- [16] N.T. Wright. Quantitative models of thermal damage to cells and tissues. In *Heat Transfer and Fluid Flow in Biological Processes*, pages 59–76. Elsevier, 2015.
- [17] M.H. Niemz. *Laser-tissue interactions: fundamentals and applications*. Springer Science & Business Media, 2013.
- [18] F. Petrella, S. Cavaliere, and L. Spaggiari. Popcorn effect. *Journal of Bronchology & Interventional Pulmonology*, 20(2):193–194, 2013.
- [19] R.M. Verdaasdonk, C. Borst, and M.J.C. Van Gemert. Explosive onset of continuous wave laser tissue ablation. *Physics in Medicine & Biology*, 35(8):1129, 1990.
- [20] A. Vogel and V. Venugopalan. Mechanisms of pulsed laser ablation of biological tissues. *Chemical Reviews*, 103(2):577–644, 2003.
- [21] A.L. McKenzie. Physics of thermal processes in laser-tissue interaction. *Physics in Medicine & Biology*, 35(9):1175, 1990.
- [22] M. Gerstmann, Y. Linenberg, A. Katzir, and S. Akselrod. Char formation in tissue irradiated with a CO₂ laser: model and simulations. *Optical Engineering*, 33(7):2343–2352, 1994.
- [23] A.L. McKenzie. A three-zone model of soft-tissue damage by a CO₂ laser. *Physics in Medicine & Biology*, 31(9):967, 1986.
- [24] A. Sagi, A. Avidor-Zehavi, A. Shitzer, M. Gerstmann, S. Akselrod, and A. Katzir. Heating of biological tissue by laser irradiation: temperature distribution during laser ablation. *Opt. Eng.*, 31(7):1425–1431, 1992.
- [25] J.A. Pearce. Relationship between arrhenius models of thermal damage and the cem 43 thermal dose. In *Energy-based Treatment of Tissue and Assessment V*, volume 7181, page 718104. International Society for Optics and Photonics, 2009.
- [26] F.C. Jr Hendriques. Studies of thermal injury; the predictability and the significance of thermally induced rate processes leading to irreversible epidermal injury. *Arch. Pathol.(Chic)*, 43:489–502, 1947.
- [27] S.C. Jiang, N. Ma, H.J. Li, and X.X. Zhang. Effects of thermal properties and geometrical dimensions on skin burn injuries. *Burns*, 28(8):713–717, 2002.
- [28] K.R. Diller and L.J. Hayes. A finite element model of burn injury in blood-perfused skin. *Journal of Biomechanical Engineering*, 105(3):300–307, 1983.
- [29] H. Ye and S. De. Thermal injury of skin and subcutaneous tissues: A review of experimental approaches and numerical models. *Burns*, 43(5):909–932, 2017.

- [30] I.V. Meglinski and S.J. Matcher. Quantitative assessment of skin layers absorption and skin reflectance spectra simulation in the visible and near-infrared spectral regions. *Physiological Measurement*, 23(4):741, 2002.
- [31] B.R. Loiola, H.R.B. Orlande, and G.S. Dulikravich. Thermal damage during ablation of biological tissues. *Numerical Heat Transfer, Part A: Applications*, pages 1–17, 2018.
- [32] Alma Lasers. Pixel CO2, 2018.
- [33] D.J. Segelstein. *The complex refractive index of water*. PhD thesis, University of Missouri–Kansas City, 1981.
- [34] M. Lapidoth, S. Halachmi, S. Cohen, and D.B. Amitai. Fractional co2 laser in the treatment of facial scars in children. *Lasers in Medical Science*, 29(2):855–857, 2014.
- [35] M.A. Trelles, M. Shohat, and F. Urdiales. Safe and effective one-session fractional skin resurfacing using a carbon dioxide laser device in super-pulse mode: a clinical and histologic study. *Aesthetic Plastic Surgery*, 35(1):31–42, 2011.
- [36] E. Kohl, J. Meierhöfer, M. Koller, F. Zeman, L. Groesser, S. Karrer, U. Hohenleutner, M. Landthaler, and S. Hohenleutner. Fractional carbon dioxide laser resurfacing of rhytides and photoaged skin—a prospective clinical study on patient expectation and satisfaction. *Lasers in Surgery and Medicine*, 47(2):111–119, 2015.